Earth Planet. Sci. Lett. 648 (2024) 119098

Contents lists available at ScienceDirect

Earth and Planetary Science Letters

journal homepage: www.elsevier.com/locate/epsl

# Stable silicon isotope fractionation reflects the routing of water through a mesoscale hillslope

Andrew Guertin [a,*], Charlie Cunningham [b], Julien Bouchez [c], Marine Gelin [c], Jon Chorover [b], Hannes Bauser [d], Minseok Kim [e], Peter Troch [b], Louis A. Derry [c,f], Jennifer L. Druhan [a,c]

[a] University of Illinois Urbana-Champaign, Urbana, IL, United States
[b] University of Arizona, United States
[c] Université Paris Cité, Institut de Physique du Globe de Paris, CNRS, France
[d] University of Nevada Las Vegas, United States
[e] Pusan National University, South Korea
[f] Cornell University, United States

ARTICLE INFO

Editor: Dr H Bao

ABSTRACT

Concentration - isotope Ratio - Discharge (C-R-Q) relationships offer a promising means of disentangling the underlying hydrologic, geochemical, and ecological factors that produce variations in stream solute chemistry across a variety of critical zone systems. However, natural environments are both temporally and spatially complex, and prevailing interpretations of these C-R-Q patterns remain difficult to validate. Here we employ three replicate artificially constructed hillslopes at the Landscape Evolution Observatory (LEO) in Tucson, Arizona as simplified analogs to natural catchments. LEO allows us to record silicon stable isotope ($\delta^{30}$Si) signatures of fluid discharge under a controlled irrigation schedule in a system devoid of vegetation. This unique meso-scale experiment enables, for the first time, evaluation of metalloid stable isotope signatures at the scale of natural hillslopes constrained to known fluid transit time distributions (TTDs) and limited to fractionation in association with secondary mineral formation. We report $\delta^{30}$Si in discharge samples collected over three randomized storm events of varying intensity. The data reflect consistent enrichment in the fluid phase between +1.00 and +2.07 ‰ across the three hillslopes, despite highly variable irrigation scenarios, reflecting substantial loss of $SiO_2$ from solution due to secondary mineral precipitation. We compare results from an isotope-enabled Reactive Transport Model (RTM) and the discharge measurements from LEO to constrain the contributions of both characteristic watershed TTDs and fractionation pathways in emergent $\delta^{30}$Si signatures. Our study confirms and expands upon recent work in natural systems attributing intra-site variability in silicon stable isotope signatures to the routing of fluid through catchments.

## 1. Introduction

Meteoric water actively circulates in the shallow subsurface layers of upland watersheds, subject to extraction by vegetation and drained to the headwaters of rivers. Rock-derived solutes are released as precipitation infiltrates through shallow, organic-rich soils, contacting and equilibrating with an elevated $pCO_2$ environment to create the potential for fluid-rock weathering reactions. Over geologic timescales, this linkage allows silicate weathering to extract $CO_2$ from the atmosphere, regulating atmospheric greenhouse gas levels (Caves Rugenstein et al., 2019; Mackenzie and Garrels, 1966; Raymo and Ruddiman, 1992; Urey and Korff, 1952; Walker et al., 1981). Upland watersheds are commonly considered “hotspots” of silicate weathering (Bluth and Kump, 1994; Brantley et al., 2023; Deng et al., 2022; Drever and Clow, 1995; Drever and Zobrist, 1992; Mcclain et al., 2003; Millot et al., 2002; Oliva et al., 2003; Stallard, 1985; Stallard and Edmond, 1983, 1987; White et al., 1999) but the linkages between these weathering rates and the pace and timing of fluid storage and drainage through the shallow subsurface remain poorly known.

Fluid travel time distributions (TTDs) dictate the duration fluid spends in contact with minerals (Maher, 2010, 2011). The ensemble of these pathways that emerge as springs and streams encompasses a range

---

* Corresponding author.
*E-mail address:* andrew58@illinois.edu (A. Guertin).

https://doi.org/10.1016/j.epsl.2024.119098
Received 25 July 2024; Received in revised form 19 October 2024; Accepted 26 October 2024

of water ages dependent on the interior structure, hydrologic storage, flow path and antecedent conditions of a given watershed. Across a wide variety of settings, streams are commonly composed of relatively young water, but the mean and shape of the fluid age distribution is highly variable due to a variety of forcing parameters including seasonality, storm events and ecosystem water demand (Birkel et al., 2015; Hrachowitz et al., 2015; Knapp et al., 2019; Marçais et al., 2022; Soulsby et al., 2015; Tetzlaff et al., 2014; Von Freyberg et al., 2018; Wilusz et al., 2017). These natural variations are now being overprinted by rapidly changing climate patterns which are intensifying storm events, prolonging periods of drought, and evolving seasonal regimes (Intergovernmental Panel on Climate, 2023).

Parsimonious hydrologic modeling frameworks, such as StorAge Selection (SAS) functions, are increasingly adept at capturing such transient water age distributions (Harman, 2015; Harman and Kim, 2014), but extensions of these models to interpret solute geochemistry are only just emerging (Benettin et al., 2015; Hrachowitz et al., 2016; Kirchner and Neal, 2013; Li et al., 2021; Rinaldo et al., 2015; Van Der Velde et al., 2010). A major challenge is the volume average representation inherent to these frameworks, in which a given storage volume holds a variety of individual fluid parcels. Each parcel delivered into the watershed by infiltration events and each aging linearly with time until removal (e.g., evapotranspiration, discharge) from the system. In contrast, the solute concentrations of near surface water are the result of multiple coupled mineral dissolution and precipitation reactions. These reactions are often complicated by a variety of related factors including incongruent weathering, cation exchange, and nutrient cycling. These reactive pathways are heterogeneously distributed through the spatial structure of the near-surface and each act on unique timescales. Ultimately, this coupled and contemporaneous distribution of reactions complicates interpretation of observed riverine solute concentrations. For example, the concentrations of rock weathering – derived solutes often appear to remain essentially constant in stream water even as discharge varies by orders of magnitude (Floury et al., 2024; Godsey et al., 2009; Ibarra et al., 2016), an observation difficult to reproduce from a chemically homogeneous reactor (Hall, 1970, 1971). Given the unique capacity of stream solute fluxes to offer an integrated signature of internal watershed biogeochemical reactivity, quantitative and predictive frameworks describing the emergence of these signals would advance the use of stream chemistry as a diagnostic of internal Critical Zone functionality.

Certain stable isotope ratios, like those of silicon ($^{30}Si/^{28}Si$, hereafter presented as a normalized ratio $\delta^{30}Si$), offer a means of parsing through the variety of biogeochemical factors that produce stream solute concentrations. $\delta^{30}Si$ ratios are sensitive to the formation of secondary silicate minerals and ecosystem cycling (De la Rocha et al., 2000; Ziegler et al., 2005a, b). This isotope system has been extensively studied in the Critical Zone (Frings et al., 2021) as a tracer of clay formation (Georg et al., 2007), mixing of Si sources (Georg et al., 2006a), and biological uptake (Ding et al., 2004; Engström et al., 2010). In these near-surface weathering environments, new solid phases containing Si tend to preferentially incorporate the lighter $^{28}Si$ isotope, enriching the fluid in the heavier $^{30}Si$ (De La Rocha et al., 2000; Fernandez et al., 2019; Frings et al., 2015; Hughes et al., 2013). Fernandez et al. (2022) leveraged this behavior to argue that $\delta^{30}Si$ of low-order streams may reflect characteristic TTDs in watersheds. Across six diverse upland environments, each stream maintained an individual range of $\delta^{30}Si$ signatures tightly clustered around their mean value, even through major storm events. The authors hypothesized that a combination of fractionating pathways and characteristic TTDs contribute to this behavior. A subsequent modeling study by Druhan and Benettin (2023) offered a forward and process-based model to test this hypothesis. This model uses a SAS-type framework to predict stable isotope ratios as a function of fluid age distributions, such that it is capable of predicting solute $\delta^{30}Si$ values during transient events, likes storms, and periods of quiescence. The model incorporates a coupling between two reactions, one representing dissolution of primary mineral(s) and the second representing the capacity for precipitation (or re-dissolution) of secondary phases. The latter is isotopically fractionating, leading to a minimum fluid age necessary to achieve stable isotope fractionation in the model. The results produce clustered $\delta^{30}Si$ values consistent with the natural watersheds reported by Fernandez et al. (2022) as a function of the storage volume and fluid age distributions of the artificial watersheds constructed in the model.

Contemporaneous advancement of novel stable isotope tracers and models coupling fluid age distributions to weathering reactions clearly holds great potential. Here, we offer a compromise between the excessive timescales necessary to study coupled transport and reaction controls on silicate weathering in the lab (e.g., White et al., 2017) and structural, ecological and chemical complexities characteristic of natural watersheds (e.g., White et al., 2015) by utilizing the Landscape Evolution Observatory (LEO), a component of Biosphere2 operated by the University of Arizona. Unlike the upland watersheds described in Fernandez et al. (2022), LEO provides a unique opportunity to parameterize and validate the effectiveness of process-based weathering models as proposed in Druhan and Benettin (2023) through the capacity to describe isotopic signatures in a system with constrained fluid age distributions and fractionation pathway(s).

## 2. Experimental facility and methods

LEO, launched in 2012, was designed to isolate and interrogate the earliest stages of landscape development. The facility consists of three identical artificially constructed hillslopes (30 m long by 11 m wide), each tilted to an average slope of 10° A primary zone of convergence focuses water drainage towards the center of each hillslope base, extending 18 m upslope from the bottom drainage face, reaching a maximum incline of 17° The slopes are covered in 1 m of crushed basaltic tephra (Table S1), extracted from a deposit associated with the Merriam Crater in northern Arizona. The unweathered material has a loamy-sand texture with a particle size distribution of 84.6 % sand, 12.2 % silt, and 3.2 % clay. Four discrete layers, each 0.32 m thick, were sequentially added to the slope and compacted to 0.25 m. After compaction, the porous media had a bulk density of 1.59 g $cm^{-3}$ and an average porosity of 39 % (Pangle et al., 2015). Irrigation to the slopes is purified by reverse-osmosis filtration, pre-equilibrated with atmospheric $CO_2$, and applied at rates between ~3 mm $h^{-1}$ and ~40 mm $h^{-1}$. The basaltic tephra has now been exposed to these controlled weathering conditions for 12 consecutive years. LEO resides within an enclosed structure, protected from local weather, and fully equipped with a variety of meteorological and climate sensors. The surface and interior of the slopes are instrumented with a complementary range of sensors including temperature and water content (Arevalo et al., 2020; Volkmann et al., 2018).

### 2.1. Irrigation schedule

This study reports solute chemistry and $\delta^{30}Si$ ratios from a sequence of three randomized irrigation events applied equivalently to each hillslope. Each precipitation event lasted 30 days, interspersed by a dry period which progressively increased from 30 to 60 and finally 90 days to test the effect of older water on discharge chemistry (Fig. 1). During each irrigation, water was applied to the slopes on and off at varied intensities to generate a wide range of mean fluid ages and travel times and their time variability. The hourly irrigation series was randomly generated using a model based on the rainfall generation algorithm described in Robinson and Sivapalan (1996), which was modified for this experiment to exclude irrigation during nighttime and weekends.

The parameters for the irrigation probability distributions were specified to fulfill two main criteria: 1) creating significant fluctuations in the system, and 2) ensuring the maximum water table height remains below 0.7 m to prevent overland flow. Several irrigation time series

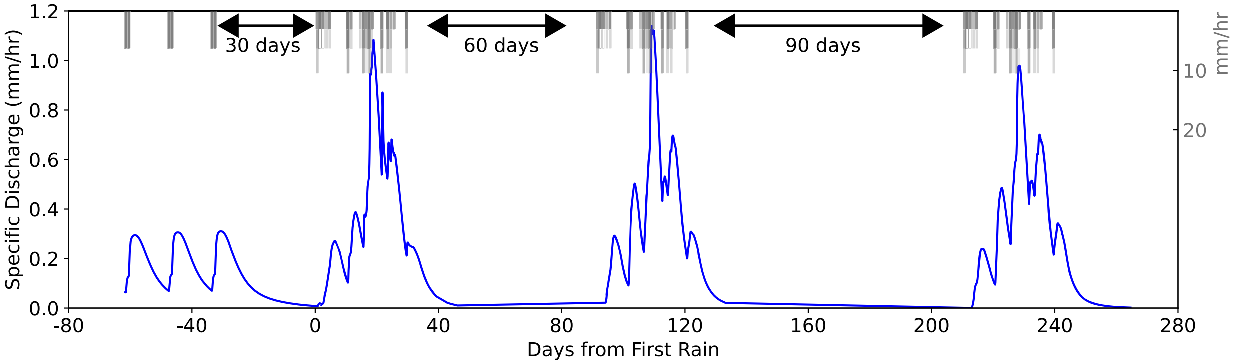

**Fig. 1.** Irrigation schedule (grey bars) with attendant seepage face discharge (blue) from the center hillslope. Note discharge from the pre-irrigations leading up to the first irrigation pulse (starting at day 0) is modeled, from day 0 onward the discharge rates are measured.

were generated and tested using the numerical model CATHY (as described by Kim (2018) and Van Den Heuvel et al. (2018) for use in LEO) to confirm they met these criteria. One time series that satisfied these conditions was selected for the experiment. The projected TTDs, were modeled based on previous studies of the system (Kim and Harman, 2022; Kim and Troch, 2020; Kim et al., 2021, 2022). For this study, we utilized the SAS function fitted to data from a previous tracer experiment described by Kim et al. (2022), to estimate the TTDs. This SAS function successfully reproduced the observed tracer breakthrough curves in a 2019 LEO experiment with a similarly generated irrigation schedule (unpublished data). The SAS function framework requires inflow and outflow data, as well as storage time series, to estimate the TTDs. We used observed data during this 2022 experiment for this purpose. Additionally, the irrigation water was spiked with a deuterium tracer to validate model projections in future work.

### 2.2. *Sampling strategy*

Discharge at the bottom seepage face of the LEO hillslopes is funneled through a trench to produce a single flux-weighted collection point (Figure S1). Over the course of the three irrigation periods, samples were collected from this point every two hours using ISCO autosamplers for each slope while the discharge faces were actively draining. ISCO collection bottles were rotated and cleaned in nitric acid between deployments. Discharge samples were filtered by hand at 0.22 µm and acidified to a pH of 3 using trace-metal grade nitric acid in a designated clean area before storage.

### 2.3. *Analytical methods*

Major cation and dissolved Si measurements were conducted at the Institut de Physique du Globe de Paris (IPGP) by inductively coupled plasma mass spectrometry using an Agilent 7900 Q-ICP-MS. Instrumental accuracy was checked using the certified river water reference standard SLRS-6 once every eight samples to check against intra-lab certified values and determine measurement uncertainty over time. Uncertainty in Si, Na, and Si/Na was propagated from two standard deviations of repeat SLRS-6 measurements throughout the course of analysis and determined to be 4.21 % for Si, 4.50 % for Na, and 4.14 % for Si/Na. Stable silicon isotope analysis was carried out at IPGP using a Thermo Finnigan Neptune plus MC-ICP-MS. A column chemistry protocol (adapted from Georg et al., 2006b; Pringle et al., 2014; van den Boorn et al., 2006) was applied to prepare samples. The technique utilizes the BioRad AG50W-X12 cation-exchange resin bed in BioRad columns. Columns are precleaned through systematic application of nitric and hydrochloric acid before adding sample and diluting to a concentration of 2 ppm Si. The technique provides near 100% Si yield through two elution steps of 2 and 3 mL MQ water. Fluid samples were injected directly into the columns. A solid sample of the basalt covering the LEO hillslopes was first prepared using alkali-fusion digestion (Georg et al., 2006) before column chemistry. A wet plasma Standard Introduction System (SIS), double Scott/cyclonic spray chamber, and a 100 µL min$^{-1}$ Teflon nebulizer were used to inject the sample into the mass spectrometer. To correct for instrumental mass bias, samples were bracketed by an internal NBS-28 standard using the standard δ notation, where $^{30}Si(\%) = \left[\left(^{30}Si/^{28}Si\right)/\left(^{30}Si\right)/\left(^{28}Si_{NBS28}\right) - 1\right]$, Four replicate measurements were taken for each sample aliquot. To ensure long term reproducibility, external Diatomite and BHVO-2 standards were run, bracketed by two NBS-28 standards, every 16 sample measurements. Each sample is recorded as an average of four measurements and reported with a 95 % confidence interval.

## 3. Results

Discharge at the terminal seepage face began ~2 days after the start of each irrigation and continued for roughly 20 – 30 days into the subsequent dry period. Over this time interval, 184 δ$^{30}$Si measurements were made spanning the three pulses (Fig. 2). The associated dissolved Si concentrations (µmol/L) remained consistent between the three hillslopes and fell in between 230 and 375 µmol/L. Across the three slopes, Si concentrations were highest during pulse 1 (342 ± 65 µmol/L). During pulse 2 (294 ± 25 µmol/L), the first fluid discharging from the seepage face showed slightly lower Si concentrations than at the end of pulse 1 and these values further declined across the duration of pulse 2 and the subsequent recession period. Concentrations dipped at the start of pulse 3 (279 ± 32 µmol/L), reaching a minimum roughly contemporaneous with peak discharge. Over the recession limb of the pulse 3 hydrograph, Si concentrations in all three hillslopes systematically increased from a minimum of 284 µmol/L to a maximum of 310 µ>mol/L measured in the last two weeks of seepage face drainage.

Fluid isotope values (Δ$^{30}$Si$_{\text{diss-rock}}$) are corrected to reflect fractionation relative to the basalt (Δ$^{30}$Si$_{\text{diss-rock}}$ = δ$^{30}$Si$_{\text{diss}}$ - δ$^{30}$Si$_{\text{rock}}$). This normalization to the bulk mineralogy is common in silicon isotope studies (e.g. Fernandez et al., 2022; Ding et al., 2004) and variability within basalts is generally quite limited (Wang et al., 2019). We use a δ$^{30}$Si$_{\text{rock}}$ ratio of −0.30 ± 0.04 ‰ based on 8 replicate measurements of the fresh basaltic tephra applied to the LEO hillslopes. All resulting Δ$^{30}$Si$_{\text{diss-rock}}$ values fell between +1.0 and +1.62 ‰, apart from one sample in pulse 1 (2.07 ± 0.05 ‰). These values indicate clear and systematic enrichment of $^{30}$Si relative to the basalt. We report two versions of the mean Si concentrations and Δ$^{30}$Si$_{\text{diss-rock}}$ ratios for each hillslope during each pulse (Table 1), (1) a standard mean value and (2) a flux-weighted mean, consistent with the typical approach used in reporting discharge-weighted solute concentrations in natural systems (Preston et al., 1989). Flux-weighted Δ$^{30}$Si$_{\text{diss-rock}}$ (‰) were similarly consistent between the three hillslopes and across each pulse.

Within each pulse, Δ$^{30}$Si$_{\text{diss-rock}}$ ratios follow a consistent pattern, illustrating a slight decrease through time from the start of the irrigation

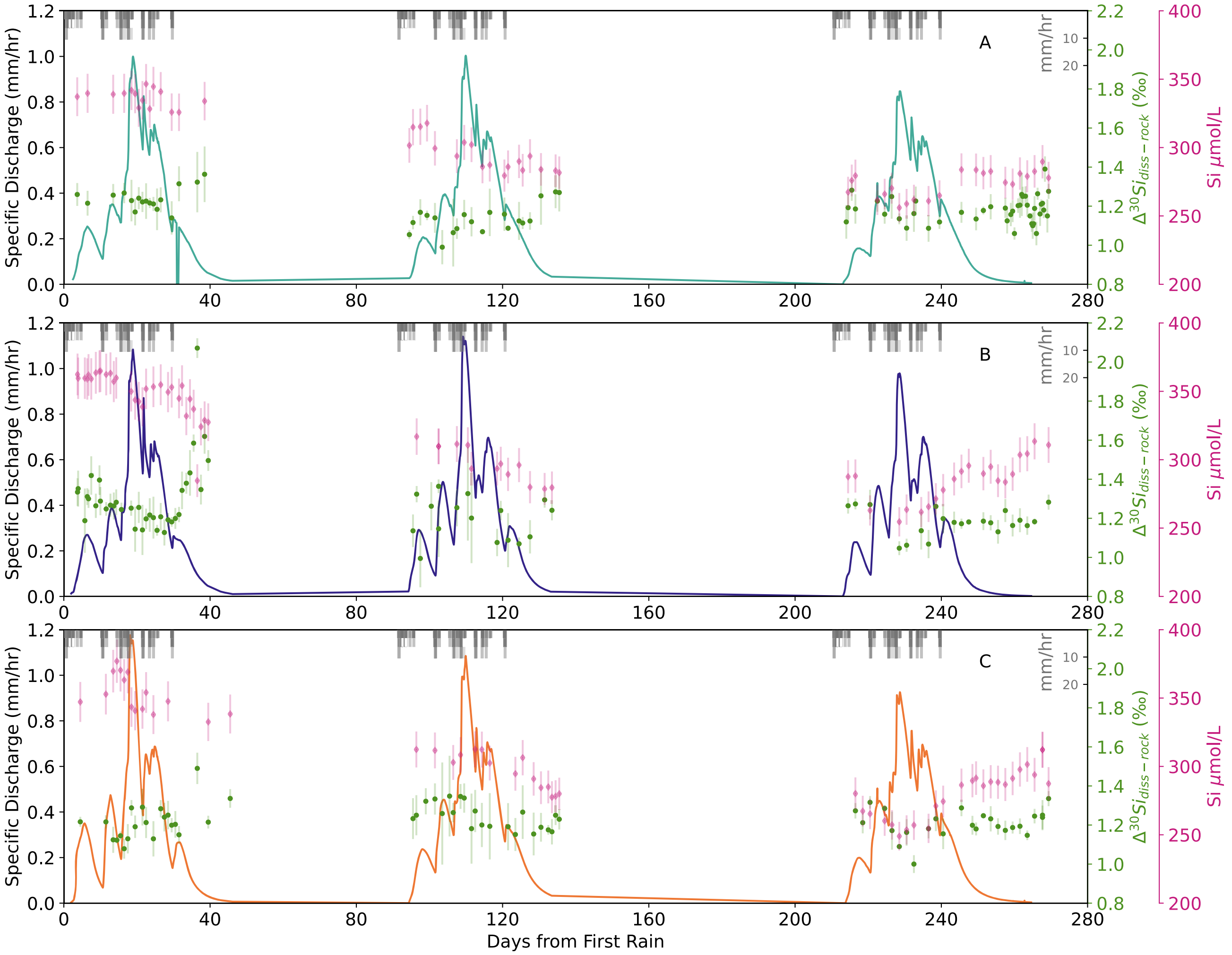

**Fig. 2.** (A) western, (B) central and (C) eastern hillslope timeseries of discharge (y1-axis), $\Delta^{30}Si_{diss-rock}$ (y2-axis), and Si µmol/L (y3-axis). Green bars represent 95 % confidence interval. Error shown on Si concentrations and isotope ratios are described in Section 2.3.

**Table 1**
Mean and (flux-weighted mean) of $\Delta^{30}Si_{diss-rock}$ (‰) for each hillslope divided by pulse.

| Slope | Pulse 1 | Pulse 2 | Pulse 3 | Overall |
|---|---|---|---|---|
| West | 1.23 ± 0.11<br>(1.22 ± 0.11) | 1.12 ± 0.14<br>(1.12 ± 0.14) | 1.18 ± 0.10<br>(1.15 ± 0.12) | 1.18 ± 0.14<br>(1.18 ± 0.13) |
| Center | 1.31 ± 0.35<br>(1.25 ± 0.40) | 1.17 ± 0.23<br>(1.18 ± 0.27) | 1.18 ± 0.14<br>(1.13 ± 0.17) | 1.25 ± 0.31<br>(1.22 ± 0.34) |
| East | 1.21 ± 0.18<br>(1.19 ± 0.19) | 1.24 ± 0.14<br>(1.27 ± 0.16) | 1.21 ± 0.14<br>(1.17 ± 0.16) | 1.22 ± 0.16<br>(1.19 ± 0.14) |

to peak discharge (Fig. 2). Following peak discharge and moving into the recession period, $\Delta^{30}Si_{diss-rock}$ values generally increase. The most extreme example of this behavior is the one very high value measured in the center hillslope during pulse 1 in the final week of drainage. There is no clear relationship between $\Delta^{30}Si_{diss-rock}$ (‰) and Si concentration (µmol/L) or $\Delta^{30}Si_{diss-rock}$ and discharge (mm/hour) across the three hillslopes or between pulses (Fig. 3). Fluid $\Delta^{30}Si_{diss-rock}$ ratios show slightly more variability in the range of discharge rates at or below 0.3 mm/hr (1.24 ± 0.25 ‰) (i.e., ~25 % of peak discharge) relative to values at or above 0.3 mm/hr (1.18 ± 0.16‰), but this is not reflected in the corresponding Si concentrations.

## 4. Discussion

### 4.1. Evidence of secondary mineral formation

Dissolved silicon concentrations alone are extremely difficult to parse, as they result from a variety of contemporaneous mineral dissolution and precipitation reactions as well as evapoconcentration and flow path mixing. Our $\Delta^{30}Si_{diss-rock}$ data offer novel evidence of clear isotopic enrichment in the dissolved Si draining from the seepage faces of the LEO hillslopes, consistent with mass-dependent isotope fractionation associated with secondary mineral formation (Bern et al., 2010; Georg et al., 2006a; Opfergelt et al., 2008; Ziegler et al., 2005a, b). Ecosystem cycling, which complicates this interpretation in natural watersheds (Frick et al., 2020; Frings et al., 2021b; Poitrasson, 2017), is not a factor at LEO. Another avenue for Si isotopic fractionation is the adsorption of Si onto oxy-hydroxide minerals (Delstanche et al., 2009; Opfergelt et al., 2009; Opfergelt and Delmelle, 2012). These studies show that adsorption of silicic acid is correlated with the extent of weathering and hence abundance of Fe and Al hydroxides. In comparison, the LEO basalts have only been subject to weathering for ~12 years. Thus far the accumulation of secondary phases, including Fe and Al oxy-hydroxides, is not yet detectable in the solid mineralogy. This leads us to rule out adsorption of Si as a significant contributor to fractionation, however, we note that contemporaneous sorption and secondary phase formation are not mutually exclusive, and it is common to

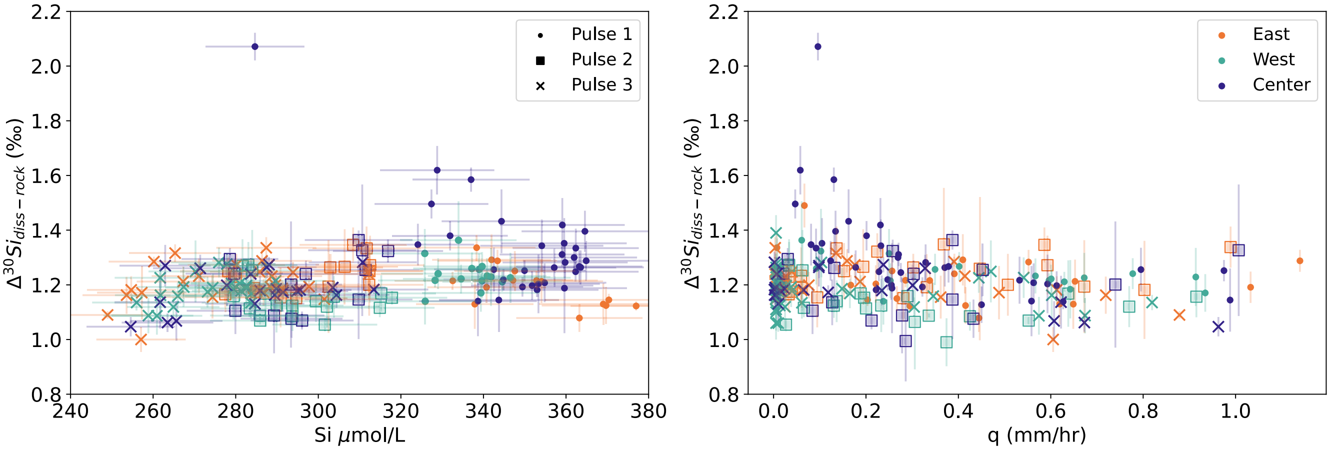

**Fig. 3.** Left $\Delta^{30}$Si$_{\text{diss-rock}}$(‰) against dissolved Si (μmol/L) Right: $\Delta^{30}$Si$_{\text{diss-rock}}$(‰) against Q (mm/hr) for all three pulses. '•' = Pulse 1, '□' = Pulse 2, 'x' = Pulse 3. Error shown on Si concentrations and isotope ratios are described in Section 2.3.

represent the two pathways in a combined fractionating reaction (e.g., Golla et al., 2021,2024). Prior studies utilizing pore water chemistry, seepage cation exports, and geochemical modeling of the LEO hillslopes support the inference that multiple secondary phases are oversaturated in solution and are likely to be actively forming (Dontsova et al., 2009; Pohlmann et al., 2016). We thus proceed by utilizing fractionation factors appropriate to represent formation of a range of common secondary silicate minerals, without ruling out the possibility for a comparatively minor extent of sorption. Field observations suggest, for example, that the formation of kaolinite exerts a similar fractionation ($\alpha = 0.9980$) (Ziegler et al., 2005b) to experimentally derived values for allophane ($\alpha = 0.9982$) (Ziegler et al., 2005a), while a wide range of values have been reported for other inorganic phases, including amorphous silica ($\alpha = 0.9970$ to 0.9990) (Fernandez et al., 2019; Geilert et al., 2014; Roerdink et al., 2015; Yanhe et al., 1995) depending on experimental conditions.

If secondary mineral formation is as prevalent across the hillslopes as our $\Delta^{30}$Si$_{\text{diss-rock}}$ values would suggest, then Si concentrations should be depleted in the seepage face fluids relative to elements not retained in these new solids. Sodium (Na) is generally excluded from common secondary mineral phases which form in upland watersheds (Dellinger et al., 2015; Georg et al., 2007; Gislason et al., 1996; Millot et al., 2010). Assuming variations in Na concentration are solely attributable to the balance between basalt dissolution rates and the rates of fluid drainage through the hillslopes, then changes in Si/Na must reflect additional reactive pathways influencing dissolved silica concentrations. As done in previous studies (Brichau et al., 2008; Charbonnier et al., 2024; Fernandez et al., 2022; Georg et al., 2006a; Gislason et al., 1996), the solute to Na ratio is further normalized to the bedrock stoichiometry (Eq. (1)).

$$f^{Si}_{diss} = \frac{\left(\frac{Si}{Na}\right)_{discharge}}{\left(\frac{Si}{Na}\right)_{bedrock}} \qquad (1)$$

The result is a metric for once-dissolved Si lost to secondary phases relative to congruent dissolution. For the LEO basalt, we consider two definitions of $\left(\frac{Si}{Na}\right)_{bedrock}$, one based on the bulk solid (8.41; Table S1) and another based on the fraction of this bulk composed of basaltic glass (6.92; Table S1). Basaltic glass is highly reactive (Pohlmann et al., 2016), and commonly considered the most relevant primary phase involved in basaltic weathering systems (Brichau et al., 2008; Georg et al., 2006a; Gislason et al., 1996). Basalt $\delta^{30}$Si values are generally quite consistent regardless of glass fraction (Savage et al., 2010), and here we assume that the bulk LEO basalt reasonably reflects the effective isotopic composition of the primary minerals dissolving into the fluid phase. In what follows, we proceed with $f^{Si}_{diss}$ estimates based on the glass ratio, recognizing that this offers a more conservative estimate of Si-bearing secondary phase incorporation than the bulk basalt.

The resulting $f^{Si}_{diss}$ values indicate consistently low Si/Na ratios compared to the bedrock in fluids draining from the hillslopes (0.12 ± 0.02), suggesting loss of Si from solution into new secondary phases. This is further supported by the large enrichment in $\delta^{30}$Si$_{\text{diss-rock}}$ between the fluid and bedrock observed in our samples. We conclude that, given the lack of vascular plants or significant oxy-hydroxide content, secondary phase precipitation is the only reasonable process that could drive both Si/Na and $\Delta^{30}$Si$_{\text{diss-rock}}$ as measured in our discharge samples.

In comparison to Si concentrations, $f^{Si}_{diss}$ values show more systematic variation with discharge, peaking shortly after max discharge and then steadily declining over the recession period (Fig. 4). The general trend through time in $f^{Si}_{diss}$ is similar between hillslopes, but again unlike Si concentrations there are small systematic differences between hillslopes. This is most visible during the third pulse, where the center slope has the greatest $f^{Si}_{diss}$ and the west slope has the weakest Si depletion. Given that Si concentration timeseries are so consistent across the three hillslopes (Fig. 2), this $f^{Si}_{diss}$ variation is clearly attributable to differences in Na concentrations, suggesting that secondary phase formation buffers variations in Si concentrations while Na is more responsive to shifting balances between basalt mineral dissolution rates and fluid drainage rates. Hence, subtle differences in the drainage patterns of are more evident in their resulting Na concentrations (and $f^{Si}_{diss}$ ratios) than in their Si concentration patterns. In the center hillslope, discharge during both pulse 2 and 3 reaches a higher maximum flow rate and recedes faster than the other hillslopes. Sodium concentrations in the center slope are correspondingly lower over this high-flow period, suggesting kinetic limitation in the production of these Na concentrations over the ~30 m maximum flow path length of LEO (Figure S2). These lower Na values drive the $f^{Si}_{diss}$ of the center hillslope higher than both east and west through pulses 2 and 3. In all three hillslopes, Na increases with the mean fluid age of discharge (Figure S3).

### 4.2. Comparison to natural systems

$\Delta^{30}$Si$_{\text{diss-rock}}$ values are consistently enriched and $f^{Si}_{diss}$ values are consistently depleted, yet within these data there is no clear trend across the duration of the experiment (Fig. 5). Within and between the three irrigation pulses, discharge varied significantly while $\Delta^{30}$Si$_{\text{diss-rock}}$ remains largely stable. There exists no clear relationship between $\Delta^{30}$Si$_{\text{diss-}}$

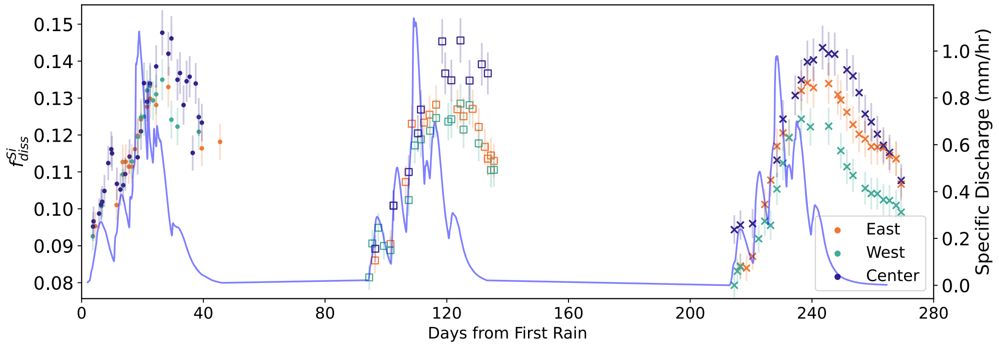

**Fig. 4.** Timeseries of $f^{Si}_{diss}$ and discharge (Q) for all three pulses on the center hillslope. '•' = Pulse 1, '□' = Pulse 2, 'x' = Pulse 3. Error shown for $f^{Si}_{diss}$ is described in Section 2.3.

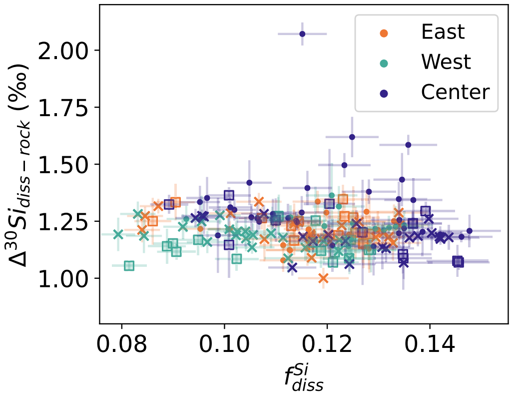

**Fig. 5.** $\Delta^{30}Si_{diss\text{-}rock}$ on the y-axis, $f^{Si}_{diss}$ of all three pulses on the x-axis. '•' = Pulse 1, '□' = Pulse 2, 'x' = Pulse 3. Error shown for Si isotope ratios and $f^{Si}_{diss}$ is described in Section 2.3.

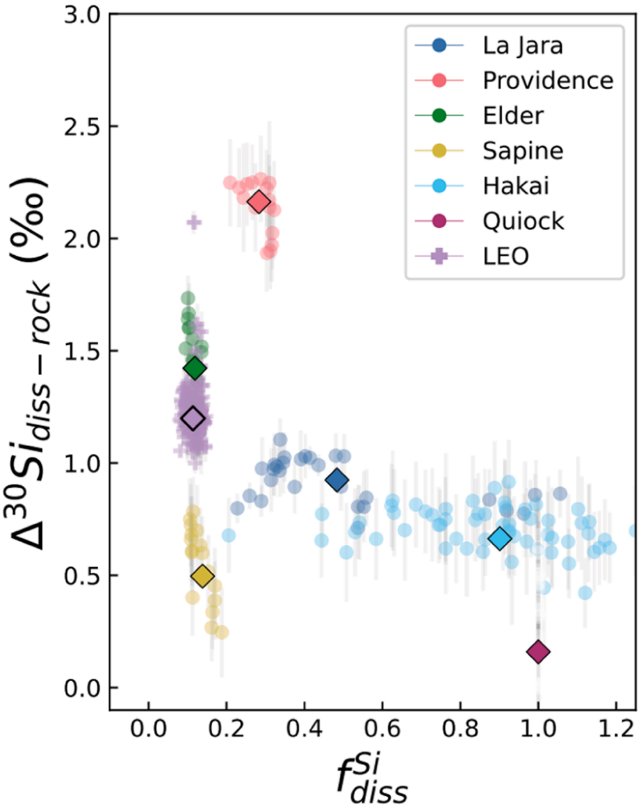

**Fig. 6.** LEO Si measurements plotted together with results from Fernandez et al. (2022). Individual measurements are shown as points, flux-weighted averages are shown as diamonds.

rock and either discharge magnitude, Si concentration, or $f^{Si}_{diss}$. This stability in $\Delta^{30}Si_{diss\text{-}rock}$ independent of discharge is consistent with observations in natural watersheds (Fernandez et al., 2022). Despite the variability in climate and lithology between sites, Fernandez et al. (2022) showed that a variety of low-order watersheds each exhibit a $\Delta^{30}Si_{diss\text{-}rock}$ signature across variations in discharge and Si depletion (Fig. 6). When contrasted against natural systems, LEO shows $\Delta^{30}Si_{diss\text{-}rock}$ and $f^{Si}_{diss}$ values similar to Elder Creek (California, USA) though this site is underlain by a shale lithology and hosts a mature evergreen forest. LEO, an artificial representation of a zero-order basin, lacks the complexities inherent to these natural systems, and we draw no specific meaning from the apparent similarity between LEO and Elder Creek. However, we do emphasize the overall consistency in $\Delta^{30}Si_{diss\text{-}rock}$ between LEO and low-order natural systems, which suggests that these experiments are a close representation of natural low-order hillslope structure and geochemical function. This consistency further supports the inference that models developed at LEO to examine the relationship of Si fractionation to TTD can reasonably be extrapolated to interpret natural watersheds.

### 4.3. Description of age distribution-based model

To interpret $\Delta^{30}Si_{diss\text{-}rock}$ signatures in upland watersheds, Fernandez et al. (2022) applied a single reaction model (Eq. (2)) coupled to a variety of TTD functional forms as well as a combination of secondary mineral and ecological fractionation pathways. In this framework, Si concentration is assumed to start from an initial value $C_0$ and decrease with time $t$ due to secondary phase precipitation and plant uptake following first-order kinetics (rate constant $k$):

$$C(t) = C_0 * exp\,(-kt) \tag{2}$$

As Na is assumed to remain unaffected by this process, $f^{Si}_{diss}$ follows the same exponential decrease as $C(t)$ and is embedded in Eq. (3). The relationship between fractionation in the fluid phase and $f^{Si}_{diss}$ is then defined using a simple Rayleigh equation:

$$\Delta^{30}Si_{diss-rock} = 1000 * (a_x - 1) * ln\left(f^{Si}_{diss}\right) \tag{3}$$

where $a_x$ is the fractionation factor associated with either secondary mineral precipitation ($\alpha_{sec}$ = 0.9980 Fernandez et al., 2019; Geilert et al., 2014; Roerdink et al., 2015; Yanhe et al., 1995; Ziegler et al., 2005) or plant uptake ($\alpha_{bio}$ = 0.99924, Ding et al., 2008; Frick et al., 2020; Opfergelt, 2010; Sun et al., 2008, 2016). For LEO, there is no significant Si loss due to plant uptake.

#### 4.3.1. Constraining a TTD for LEO

Here, this model is adapted to the TTD appropriate for the LEO experiments. Prior to the start of irrigation, expected TTDs for the LEO experiment were modeled based on past studies at the site (Kim and Harman, 2022; Kim and Troch, 2020; Kim et al., 2021, 2022). TTDs for LEO are generally weighted towards a more uniform distribution of fluid ages relative to those characteristic of natural watersheds (Kirchner et al., 2000, 2001; Mcguire et al., 2005). Distributions are consistent between hillslopes and maintain the same general structure throughout the three pulses. As a starting point, we generate a characteristic projected LEO TTD based on the mean shape of TTDs spread across the three pulses at 4-hour intervals (Fig. 7 left and Figure S4). For each 4-hour timestep during the experiment, the individual TTD is distributed around the mean fluid-age specific to that time interval. The contribution of each fluid age about this mean value is then weighted (Fig. 7 right). All individual TTDs are then averaged to generate a representative characteristic TTD for LEO. We used this characteristic TTD to age-weight the corresponding concentration and isotope ratios, which combine to create flux-weighted values representative of those exiting the discharge face. For each mean age in the range relevant to the LEO experiment, the TTD is used to weigh the contributions of water younger and older than the mean (Fig. 7 right).

#### 4.3.2. Inconsistency with Rayleigh fractionation

Si isotope signatures and $f_{diss}^{Si}$ values from the model were weighted according to the characteristic LEO TTD (Section 4.3.1) and compared against curves constrained for natural watersheds reported by Fernandez et al. (2022). Most of the Fernandez et al. (2022) data fall in a solution space of flux-weighted $\Delta^{30}\mathrm{Si}_{\text{diss-rock}}$ and $f_{diss}^{Si}$ which suggest TTDs that are strongly skewed towards young water, e.g. can be represented by exponential and gamma distributions. In comparison, the LEO Si data plot near those of Elder Creek (Fig. 6), but an exponential TTD, as suggested for Elder Creek, is not valid for LEO (Fig. 7). Instead, the comparatively uniform TTDs generated in LEO produce piston-like flow relative to the natural watersheds, leading to the necessity of an $\alpha = 0.9995$ to produce a Rayleigh-based Si fractionation vs $f_{diss}^{Si}$ curve that agrees with the experimental data (Fig. 8 left, red line). A fractionation factor so close to 1.0 is unrealistic for Si removal by kinetically-limited secondary mineral formation (Fernandez et al., 2019; Geilert et al., 2014; Roerdink et al., 2015; Yanhe et al., 1995). These results suggest a simple Rayleigh distillation model, as used in Fernandez et al. (2022), is inadequate to explain LEO Si fractionation as a function of Si depletion.

### 4.4. Multi-reaction model

We next turn to a more recent multi-reaction system developed by Druhan and Benettin (2023) where *C(t)* is calculated as:

$$C(t) = C_{LIM} + (C_0 - C_{LIM})\exp\left(-\frac{k_{eff}}{C_{LIM}}t\right) \tag{4}$$

Here $C_{LIM}$ is a maximum concentration achievable for the relevant solute in a parcel of fluid given sufficient reaction time:

$$C_{LIM} = \frac{\mathrm{k}_1 + k_2}{\left(\frac{k_1}{C_{lim1}}\right) + \left(\frac{k_2}{C_{lim2}}\right)} \tag{5}$$

and the rate at which a solute approaches this $C_{LIM}$ value is dependent on a kinetic rate constant, $k_{eff}$:

$$k_{eff} = k_1 + k_2 \tag{6}$$

This approach is based on a coupled set of dissolution and precipitation reactions, each with their own independent $C_{lim\_i}$ and $k_i$, that in combination yield a concentration $C_{LIM}$ resulting from dynamic equilibrium. A complete derivation and demonstration of appropriate behavior can be found in Druhan and Benettin (2023).

At any given time, the total concentration, $C$, is the sum of a heavy isotope, ${}^{h}C$ and a light isotope, ${}^{l}C$,

$$C = {}^{h}C + {}^{l}C \tag{7}$$

with each isotope concentration determined using the same function as Eq. (4):

$${}^{l}C(t) = {}^{l}C_{LIM} + \left({}^{l}C_0 - {}^{l}C_{LIM}\right)\exp\left(-\frac{{}^{l}k_{eff}}{{}^{l}C_{LIM}}t\right) \tag{8a}$$

$${}^{h}C(t) = {}^{h}C_{LIM} + \left({}^{h}C_0 - {}^{h}C_{LIM}\right)\exp\left(-\frac{{}^{h}k_{eff}}{{}^{h}C_{LIM}}t\right) \tag{8b}$$

The fractionation factor between the two isotopes, $\alpha_i$, sets the ratio of the light and heavy rate constants:

$$\alpha_i = \frac{{}^{h}k_i}{{}^{l}k_i} \tag{9}$$

For the present application, $k_{eff}$, $\alpha_i$ , and $C_{LIM}$ were calibrated using data from our LEO experiment (see Text S1 for full calibration process). We set the first parameter set (reaction 1) such that it is always dissolving, $C_{lim\_1} = 3500$ μmol/L and ${}^{l}\mathrm{k}_1 = 0.00180$ μmol/h, and assign $\alpha_1 =$

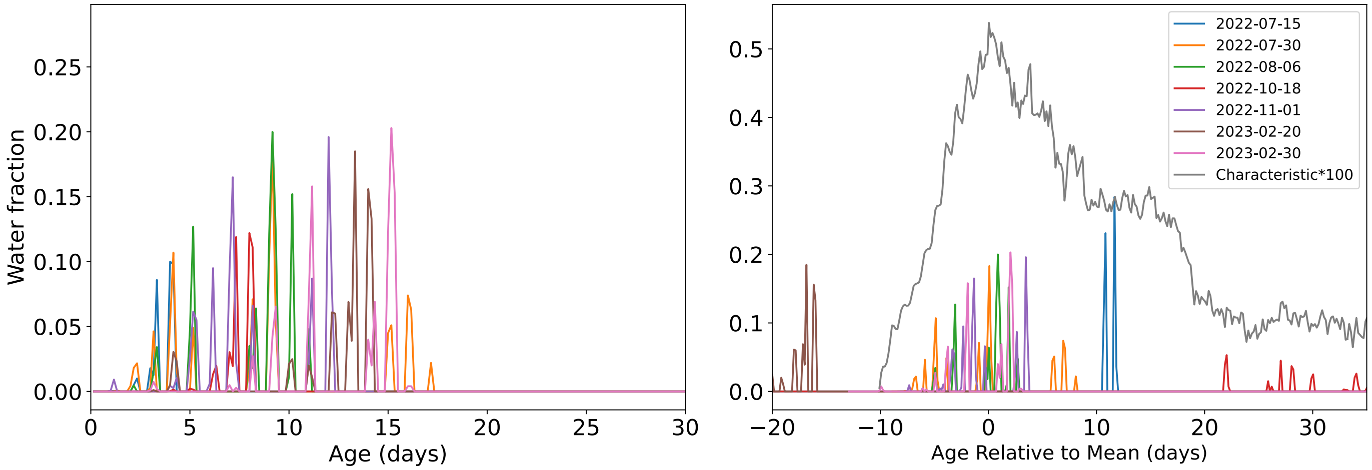

**Fig. 7.** Left: Modeled water transit time distributions at LEO for individual points in time. The Y-axis (water fraction) indicates the contribution of waters of a given age. Right: Same distributions plotted as age contributions relative to the mean age at the given time. Negative ages are contributions of water younger than the mean; positive ages are contributions of water older than the mean. Characteristic TTD scaled by 100 to show shape on same axis as individual TTDs.

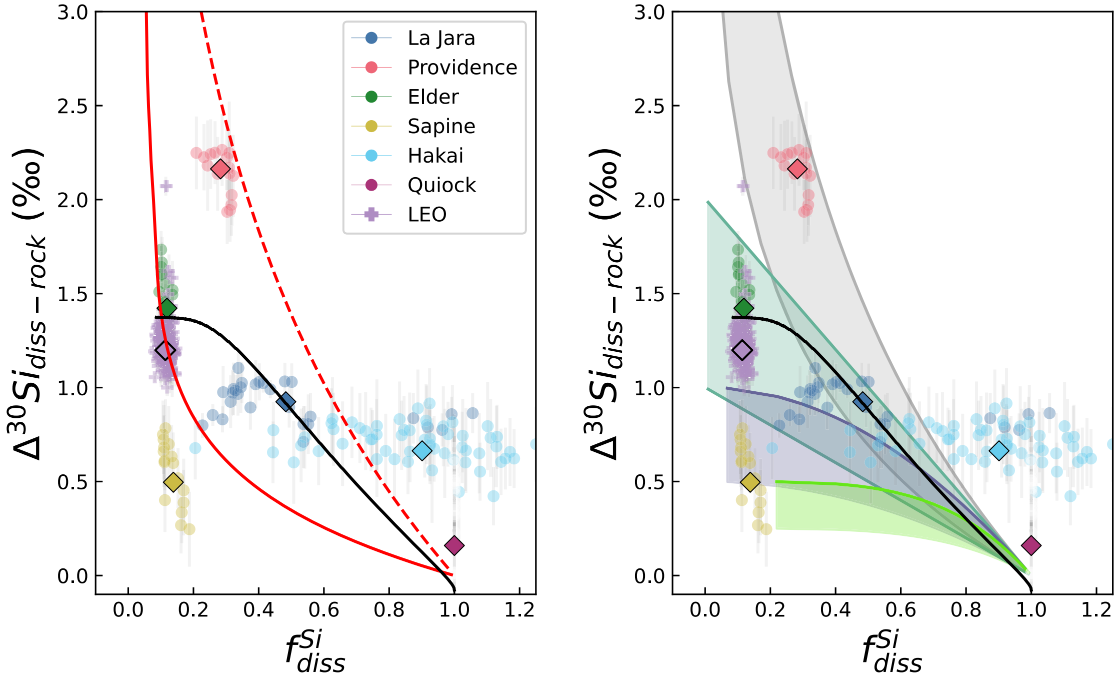

**Fig. 8.** Left: Figure 6 now with the addition of two single reaction LEO TTD models, one using α = 0.9995 (solid red line) and one using α = 0.9985 (dashed red line). The multi-reaction LEO TTD model using α = 0.9985 is given in the black line. Right: Shaded regions represent various TTDs, taken from Fernandez et al. (2022). Grey: uniform piston flow, Cyan: Exponential, Blue: Gamma (a=0.5), Green: Gamma (a=0.25). Upper bound is clay formation (α = 0.9980) and lower bound is biological uptake (α = 0.99924).

1 assuming isotope fractionation during dissolution of the basalt is negligible compared to secondary mineral formation (Chemtob et al., 2015). Reaction 2 is parameterized such that, once $C_{lim\_2}$ is exceeded, it operates as a representation of secondary mineral precipitation. Here we use $C_{lim\_2}$ = 50 μmol/L and $^{1}k_2$ = 0.0232 μmol/h, $\alpha_2$ = 0.9985. We run two versions of this model, one that produces a time series of concentrations for the heavy and light isotopes of Si, and a second that mimics a non-precipitating conservative element ($C_{NP}$) that is only subject to dissolution, as a representation of the behavior of Na. This approach allows us to calculate an appropriate value of both the Si isotope ratio and $f^{Si}_{diss}$ (Druhan and Benettin, 2023). To calculate both parameters, we use the single characteristic TTD we constrained for these LEO experiments (Section 4.3.1) to produce a weighted concentration and isotope signature for each contributing fluid age about a given mean value. The sum of these weighted contributions yields the ensemble $f^{Si}_{diss}$ and $\Delta^{30}Si_{diss-rock}$ values for a given mean fluid age. This calculation is repeated for each mean age, ranging from 0 to one year (Fig. 8, black line). The result yields close agreement with our measured values from LEO.

### 4.5. Model reproduction of observations

Reproducing $\Delta^{30}Si_{diss\text{-}rock}$ values comparable to the LEO dataset for a given $f^{Si}_{diss}$ using the single reaction model, as in Fernandez et al. (2022), requires fixing the fractionation factor to an unreasonable value: α = 0.9995 (Fig. 8). This is because a basic Rayleigh distillation model produces an exponential increase in fluid $\delta^{30}Si$ with reaction progress as Si is lost to secondary phases. For this type of model to produce a stable $\Delta^{30}Si_{diss\text{-}rock}$ signature, the system requires a more skewed weighting of fluid ages, e.g. towards younger water, such as a gamma distribution (Fig. 8). In LEO, where the age distribution is more uniform, this modeling structure reverts to a simple piston flow or space for time equivalency, and hence exponential growth of fluid $\delta^{30}Si$ values. Our results demonstrate that in the simplified watershed representation afforded by LEO, a single Rayleigh distillation model is inadequate to explain observed fluid $\delta^{30}Si$ isotope signatures.

In comparison, a coupled two-reaction model offers an inherently stabilizing behavior for both isotope fractionation and $f^{Si}_{diss}$, even when subject to piston flow. This approach is able to reproduce the $\Delta^{30}Si_{diss\text{-}rock}$ signature of LEO using both a realistic fractionation factor (0.9985) for the reaction capable of forming secondary phases (Fernandez et al., 2019; Geilert et al., 2014; Roerdink et al., 2015; Yanhe et al., 1995; Ziegler et al., 2005) and the average TTD constrained for the LEO hillslopes (Fig. 8). This result supports the inference that a highly reactive system like LEO, where fluid Si/Na ratios are low, should be characterized by a stable fluid $\delta^{30}Si$ signature that reflects a balance between contemporaneous dissolution and secondary mineral formation. The agreement between the LEO discharge and the two-reaction model suggests that this newer model may be more appropriate to constrain the isotope-water age relationship in natural systems than the previously employed Rayleigh approach.

We next consider the capacity for the two-reaction model to describe the range of $\Delta^{30}Si_{diss\text{-}rock}$ and $f^{Si}_{diss}$ observed in discharge over the course of the LEO experiments. Two principal factors are considered: the range of TTDs generated in the hillslopes during the three irrigation pulses and the range of fractionation factors suggested for $\delta^{30}Si$ during secondary mineral precipitation. Modeled TTDs for each pulse depend on the individual irrigation patterns but maintain a mostly uniform shape about their mean (Fig. 7 Right). Water from previous irrigations remains in the hillslope during dry periods and emerges in the earliest discharge produced by the next irrigation pulse (Figure S5). This leads to a range of fluid ages in the discharge exiting the hillslopes that generally increase from pulse 1 to 3 even though the TTD remain consistent across all three irrigation periods. The range of fractionation factors expected to influence fluid $\delta^{30}Si$ is dependent on which secondary phases actively precipitate from solution (Section 4.1). As flow rates and water table heights fluctuate over the course of our irrigation experiment, the dominant secondary phases precipitating from solution could vary, leading to minor fluctuations in $\delta^{30}Si$.

Applying the full range of modeled TTDs rather than an average

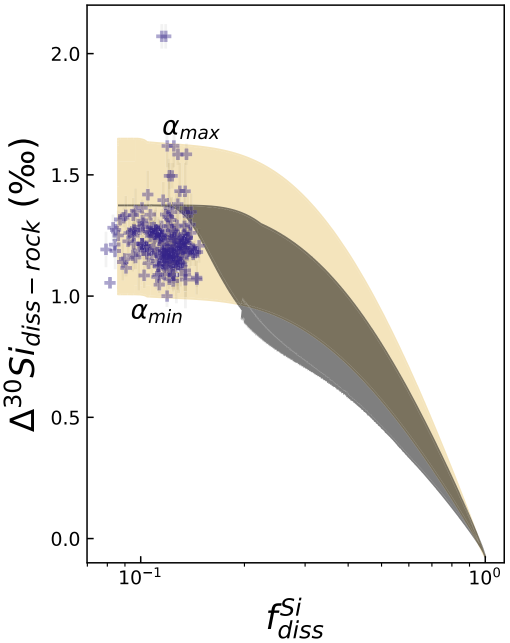

**Fig. 9.** Range of TTDs from oldest mean age (bottom line) to youngest (top line) during pulses of LEO shaded in grey using the multi-reaction model and an $\alpha = 0.9985$ for secondary mineral precipitation. In comparison, a single mean TTD for LEO, shaded in tan, is used in conjunction with a range of secondary mineral fractionation factors from $\alpha_{max} = 0.9982$ to $\alpha_{min} = 0.9989$.

yields clear variation in the Si isotopic signature as a function of $f^{Si}_{diss}$ (Fig. 9, grey shaded area). Application of the mean TTD in conjunction with an appropriate range of fractionation factors produces a generally comparable variation in Si isotope ratios (Fig. 9, tan shaded area). However, the capacity for these two variables to affect the Si isotopic signature is not equal across the range of $f^{Si}_{diss}$ from purely congruent dissolution ($f^{Si}_{diss} = 1$) to complete Si removal ($f^{Si}_{diss} = 0$). At an $f^{Si}_{diss}$ of ~0.2, both variation in the TTDs (±0.21 ‰) and in the fractionation factor (±0.32 ‰) produce a significant range of fluid $\delta^{30}$Si values (Fig. 9). However, as $f^{Si}_{diss}$ values become even lower (<0.15 for our LEO model parameterization), and fluid ages become correspondingly older, the suite of variable TTDs produces a narrower range of fluid $\delta^{30}$Si values. This is because, as the mean fluid age grows, an increasingly large proportion of the fluid that can be sampled from the hillslope has reached a stable Si concentration and isotope ratio in the two-reaction model (Figure S6). In this highly incongruent, chemically evolved signal, variation in the observed $\delta^{30}$Si ratios at these very low $f^{Si}_{diss}$ values is principally achievable through small variation in the underlying fractionation factor as a result of changes in the composition or relative distribution of actively forming secondary phases. Our LEO data falls in the range of $f^{Si}_{diss}$ values were the system appears to be transitioning away from the potential influence of variations in the TTD and towards the necessity for variations in the fractionation factor, though we strongly caution that this is a result of how the chemical reactions are parameterized in our model (Text S1) and a more detailed multi-component reaction network will be necessary to further test this behavior. Here, we show that variation in the secondary mineral fractionation factor between 0.9982−0.9989, which is well within the range previously demonstrated for common secondary phases (Fernandez et al., 2019; Geilert et al., 2014; Roerdink et al., 2015; Yanhe et al., 1995), is consistent with our data.

### 4.6. Implications for upland watersheds

Before we attempt to translate the inferences taken from these LEO experiments to natural watersheds it is critical to consider the differences between them. In hydrologic studies of fluid transit time distributions, it is common to utilize a 'fraction young water' (Fyw) based on conservative tracer transport (Benettin et al., 2022; Jasechko et al., 2016; Kirchner, 2016a, b; Lutz et al., 2018; Von Freyberg et al., 2018). Here, the comparatively fast kinetics of the fresh, minimally weathered basalt covering the LEO hillslopes supports far more rapid reaction rates than natural systems. This motivates a version of Fyw based on a threshold "fraction reaction progress" (Frp), i.e. the fraction of water exiting the system at age younger than the timescale necessary to reach $C_{LIM}$. At LEO, such a timescale would be on the order of <300 h, while natural low-order watersheds draining silicate lithology tend to be have much longer timescales (0.08 to 1+ years) (Maher, 2011). At LEO, this short characteristic reactive timescale is combined with the preference for relatively more uniform fluid ages (i.e. a higher proportion of old water for a given mean age) over a characteristic flow path, leading to pervasive production of discharge at or near $C_{LIM}$ in the competing reaction model. In a more evolved natural hillslope, longer characteristic reactive time scales lead to the capacity to produce a smaller Frp, where the solute signatures of these young waters are generally more dilute and chemodynamic. Therefore, TTDs that weigh toward inclusion of this young water should produce lower fluid $\delta^{30}$Si and $f^{Si}_{diss}$ values in discharge as well as a clearer relationship between the two weathering signatures. This inference is counterbalanced by a greater extent of geochemical evolution and structural heterogeneity encapsulated by natural hillslopes at larger characteristic sizes relative to LEO and hence the capacity to sample a much older, more geochemically evolved 'tail' in common TTD functional forms.

From this basis our study shows that a Rayleigh-type distillation model is inadequate to describe the LEO system, but it remains ambiguous whether this also undermines application to upland watersheds. Describing these watersheds with a coupled reaction model, like the one needed for LEO, inherently means that interpreting characteristic differences in stream $\delta^{30}$Si ratios depends on how the age distribution of discharge relates to the characteristic timescale necessary to reach $C_{LIM}$ in a given watershed. Fluid age distributions exert a stronger effect on $\delta^{30}$Si for the component of discharge that falls within Frp. For older water, $\delta^{30}$Si is primarily dependent on fractionation factor. LEO represents a baseline for water-rock interactions occurring within a relatively uniform hillslope. Additional factors (e.g. plant nutrient uptake, heterogeneity with depth, evapotranspiration) can disrupt this isotope to solute depletion relationship. These complicating factors preclude us from a total dismissal of Rayleigh distillation behavior in natural systems solely based on observations from LEO. However, our interpretation of the LEO Si isotope data lends support to models accounting for simultaneous mineral dissolution and precipitation in interpreting metal stable isotope signatures in the Critical Zone (e.g.,Bouchez et al., 2013). When considering the complexities of natural watersheds, more coupled datasets of fluid $\delta^{30}$Si and water age distributions are needed to extend the application of such coupled reaction models beyond LEO.

## 5. Conclusion

Simple reactive transport models have been used to link solute chemistry (Maher, 2010, 2011) and isotopic fractionation (Druhan and Benettin, 2023; Fernandez et al., 2022) to fluid age distributions. This study is the first to apply this type of isotope-enabled reactive transport model to a mesoscale system offering the capacity to constrain incongruent silicate weathering using Si isotopes for a known set of water transit time distributions. The silicon isotope values of discharge exiting the LEO hillslopes were stable across a wide range of discharge and transit times. This stability in both Si concentrations and isotope fractionation despite relatively short transit times, reflects the rapid kinetics of the fresh basalt. Two reactive transport models were tested against the LEO dataset, exposing an inability for a Rayleigh distillation framework to reach the observed relationship between Si depletion and isotope composition, due to relatively uniform, piston-like flow. These results demonstrate the need for a coupled, multi-reaction framework to describe the hydrogeochemical nature of the LEO hillslopes. While the LEO hillslopes are far more reactive and simpler in structure than typical upland watersheds, these results offer a significant attestation to the viability of multi-reaction modeling frameworks in future applications to natural systems. We thank editor Huiming Bao and three anonymous reviewers for their constructive comments.

## CRediT authorship contribution statement

**Andrew Guertin:** Writing – review & editing, Writing – original draft, Visualization, Validation, Investigation, Formal analysis, Data curation. **Charlie Cunningham:** Methodology, Data curation. **Julien Bouchez:** Writing – review & editing, Validation, Supervision, Resources, Investigation, Formal analysis, Data curation. **Marine Gelin:** Methodology, Data curation. **Jon Chorover:** Resources, Project administration, Funding acquisition. **Hannes Bauser:** Methodology, Investigation. **Minseok Kim:** Writing – review & editing, Methodology, Investigation. **Peter Troch:** Resources, Project administration, Funding acquisition. **Louis A. Derry:** Resources, Project administration, Funding acquisition. **Jennifer L. Druhan:** Writing – review & editing, Writing – original draft, Validation, Supervision, Resources, Project administration, Methodology, Investigation, Funding acquisition, Formal analysis, Conceptualization.

## Declaration of competing interest

The authors declare the following financial interests/personal relationships which may be considered as potential competing interests:

Jennifer Druhan reports financial support was provided by National Science Foundation. If there are other authors, they declare that they have no known competing financial interests or personal relationships that could have appeared to influence the work reported in this paper.

## *Acknowledgements*

This work was funded by a multi-institutional collaborative research grant awarded by the US National Science Foundation: EAR-2135405 to J.L.D.; EAR-2134453 to J.C. and P.T; EAR-2141989 to L.D. The authors thank Wei-Ren Ng, Aaron Bugaj, Eleora Jade Bailey, Anna Margaret Jones, Rhiannon Nabours, Matej Durcik, Joe Aikens, and Dani Trangmoe for their contributions to the irrigation experiment and sample collection. We thank Sofía López Urzúa, Jon Golla, Hunter Jamison, Delphine Limmois, Dimitri Rigoussen, Tu-Han Luu, Pierre Burckel, Caroline Gorge, and Laëticia Faure for assistance in analytical measurements.

## Supplementary materials

Supplementary material associated with this article can be found, in the online version, at doi:10.1016/j.epsl.2024.119098.

## Data availability

Accompanying data is available on Hydroshare at: https://doi.org/10.4211/hs.e631d6807c464f52b700cd5d9e4fbb43.

## References

Arevalo, J., Zeng, X., Durcik, M., Sibayan, M., Pangle, L., Abramson, N., Troch, P.A., 2020. Highly sampled measurements in a controlled atmosphere at the biosphere 2 landscape evolution observatory. Sci. Data 7 (1). https://doi.org/10.1038/s41597-020-00645-5.

Benettin, P., Bailey, S.W., Campbell, J.L., Green, M.B., Rinaldo, A., Likens, G.E., Botter, G., 2015. Linking water age and solute dynamics in streamflow at the Hubbard brook experimental forest, NH, USA. Water Resour. Res. 51 (11), 9256–9272. https://doi.org/10.1002/2015WR017552.

Benettin, P., Rodriguez, N.B., Sprenger, M., Kim, M., Klaus, J., Harman, C.J., Mcdonnell, J.J., 2022. Transit time estimation in catchments: recent developments and future directions. Water Resour. Res. 58 (11). https://doi.org/10.1029/2022wr033096.

Bern, C.R., Brzezinski, M.A., Beucher, C., Ziegler, K., Chadwick, O.A., 2010. Weathering, dust, and biocycling effects on soil silicon isotope ratios. Geochim. Cosmochim. Acta 74 (3), 876–889. https://doi.org/10.1016/j.gca.2009.10.046.

Birkel, C., Soulsby, C., Tetzlaff, D., 2015. Conceptual modelling to assess how the interplay of hydrological connectivity, catchment storage and tracer dynamics controls nonstationary water age estimates. Hydrol. Process. 29 (13), 2956–2969. https://doi.org/10.1002/hyp.10414.

Bluth, G.J.S., Kump, L.R., 1994. Lithologic and climatologic controls of river chemistry. Geochim. Cosmochim. Acta 58 (10), 2341–2359. https://doi.org/10.1016/0016-7037(94)90015-9.

Bouchez, J., Von Blanckenburg, F., Schuessler, J.A., 2013. Modeling novel stable isotope ratios in the weathering zone. Am. J. Sci. 313 (4), 267–308. https://doi.org/10.2475/04.2013.01.

Brantley, S.L., Shaughnessy, A., Lebedeva, M.I., Balashov, V.N., 2023. How temperature-dependent silicate weathering acts as Earth's geological thermostat. Science 379 (6630), 382–389. https://doi.org/10.1126/science.add2922.

Brichau, S., Respaut, J.-P., Monié, P., 2008. New age constraints on emplacement of the Cévenol granitoids, South French Massif Central. Int. J. Earth Sci. 97 (4), 725–738. https://doi.org/10.1007/s00531-007-0187-x.

Caves Rugenstein, J.K., Ibarra, D.E., Von Blanckenburg, F, 2019. Neogene cooling driven by land surface reactivity rather than increased weathering fluxes. Nature 571 (7763), 99–102. https://doi.org/10.1038/s41586-019-1332-y.

Charbonnier, Q., Rickli, J., Archer, C., Vance, D., 2024. The influence of secondary weathering processes on dissolved nickel isotope compositions under cold climatic conditions – Observations from the Mackenzie Basin. Geochim. Cosmochim. Acta 364, 10–21. https://doi.org/10.1016/j.gca.2023.10.026.

Chemtob, S.M., Rossman, G.R., Young, E.D., Ziegler, K., Moynier, F., Eiler, J.M., Hurowitz, J.A., 2015. Silicon isotope systematics of acidic weathering of fresh basalts, Kilauea Volcano, Hawai'i. Geochim. Cosmochim. Acta 169 (2), 63–81. https://doi.org/10.1016/j.gca.2015.07.026.

De La Rocha, C.L., Brzezinski, M.A., DeNiro, M.J., 2000. A first look at the distribution of the stable isotopes of silicon in natural waters. Geochim. Cosmochim. Acta 64 (14), 2467–2477. https://doi.org/10.1016/S0016-7037(00)00373-2.

Dellinger, M., Gaillardet, J., Bouchez, J., Calmels, D., Louvat, P., Dosseto, A., Maurice, L., 2015. Riverine Li isotope fractionation in the Amazon River basin controlled by the weathering regimes. Geochim. Cosmochim. Acta 164, 71–93. https://doi.org/10.1016/j.gca.2015.04.042.

Delstanche, S., Opfergelt, S., Cardinal, D., Elsass, F., André, L., Delvaux, B., 2009. Silicon isotopic fractionation during adsorption of aqueous monosilicic acid onto iron oxide. Geochim. Cosmochim. Acta 73 (4), 923–934. https://doi.org/10.1016/j.gca.2008.11.014.

Deng, K., Yang, S., Guo, Y., 2022. A global temperature control of silicate weathering intensity. Nat. Commun. 13 (1). https://doi.org/10.1038/s41467-022-29415-0.

Ding, T., Wan, D., Wang, C., Zhang, F., 2004. Silicon isotope compositions of dissolved silicon and suspended matter in the Yangtze River, China. Geochim. Cosmochim. Acta 68 (2), 205–216. https://doi.org/10.1016/S0016-7037(03)00264-3.

Ding, T.P., Zhou, J.X., Wan, D.F., Chen, Z.Y., Wang, C.Y., Zhang, F., 2008. Silicon isotope fractionation in bamboo and its significance to the biogeochemical cycle of silicon. Geochim. Cosmochim. Acta 72 (5), 1381–1395. https://doi.org/10.1016/j.gca.2008.01.008.

Dontsova, K., Steefel, C.I., Desilets, S., Thompson, A., Chorover, J., 2009. Solid phase evolution in the Biosphere 2 hillslope experiment as predicted by modeling of hydrologic and geochemical fluxes. Hydrol. Earth Syst. Sci. 13 (12), 2273–2286. https://doi.org/10.5194/hess-13-2273-2009.

Drever, J.I., & Clow, D.W.. (1995). Chapter 10. Weathering rates in catchments. In F. W. Arthur & L. B. Susan (Eds.), *Chemical Weathering Rates of Silicate Minerals* (pp. 463–484). De Gruyter. doi:10.1515/9781501509650-012.

Drever, J.I., Zobrist, J., 1992. Chemical weathering of silicate rocks as a function of elevation in the southern Swiss Alps. Geochim. Cosmochim. Acta 56 (8), 3209–3216. https://doi.org/10.1016/0016-7037(92)90298-W.

Druhan, J.L., Benettin, P., 2023. Isotope ratio – discharge relationships of solutes derived from weathering reactions. Am. J. Sci. 323. https://doi.org/10.2475/001c.84469.

Engström, E., Rodushkin, I., Ingri, J., Baxter, D.C., Ecke, F., Österlund, H., Öhlander, B., 2010. Temporal isotopic variations of dissolved silicon in a pristine boreal river. Chem. Geol. 271 (3), 142–152. https://doi.org/10.1016/j.chemgeo.2010.01.005.

Fernandez, N.M., Bouchez, J., Derry, L.A., Chorover, J., Gaillardet, J., Giesbrecht, I., Druhan, J.L., 2022. Resiliency of silica export signatures when low order streams are subject to storm events. J. Geophys. Res.: Biogeosci. 127 (5). https://doi.org/10.1029/2021jg006660.

Fernandez, N.M., Zhang, X., Druhan, J.L., 2019. Silicon isotopic re-equilibration during amorphous silica precipitation and implications for isotopic signatures in geochemical proxies. Geochim. Cosmochim. Acta 262, 104–127. https://doi.org/10.1016/j.gca.2019.07.029.

Floury, P., Bouchez, J., Druhan, J.L., Gaillardet, J., Blanchouin, A., Gayer, É., Ansart, P., 2024. Linking dynamic water storage and subsurface geochemical structure using high-frequency concentration-discharge records. Water Resour. Res. 60 (1). https://doi.org/10.1029/2022wr033999.

Frick, D.A., Remus, R., Sommer, M., Augustin, J., Kaczorek, D., von Blanckenburg, F., 2020. Silicon uptake and isotope fractionation dynamics by crop species. Biogeosciences 17 (24), 6475–6490.

Frings, P.J., Clymans, W., Fontorbe, G., Gray, W., Chakrapani, G.J., Conley, D.J., De La Rocha, C., 2015. Silicate weathering in the Ganges alluvial plain. Earth Planet. Sci. Lett. 427, 136–148. https://doi.org/10.1016/j.epsl.2015.06.049.

Frings, P.J., Oelze, M., Schubring, F., Frick, D.A., Von Blanckenburg, F., 2021a. Interpreting silicon isotopes in the Critical Zone. Am. J. Sci. 321 (8), 1164–1203. https://doi.org/10.2475/08.2021.02.

Frings, P.J., Schubring, F., Oelze, M., Von Blanckenburg, F., 2021b. Quantifying biotic and abiotic Si fluxes in the Critical Zone with Ge/Si ratios along a gradient of erosion rates. Am. J. Sci. 321 (8), 1204–1245. https://doi.org/10.2475/08.2021.03.

Geilert, S., Vroon, P.Z., Roerdink, D.L., Van Cappellen, P., van Bergen, M.J., 2014. Silicon isotope fractionation during abiotic silica precipitation at low temperatures: inferences from flow-through experiments. Geochim. Cosmochim. Acta 142, 95–114. https://doi.org/10.1016/j.gca.2014.07.003.

Georg, R.B., Reynolds, B.C., Frank, M., Halliday, A.N., 2006a. Mechanisms controlling the silicon isotopic compositions of river waters. Earth Planet. Sci. Lett. 249 (3), 290–306. https://doi.org/10.1016/j.epsl.2006.07.006.

Georg, R.B., Reynolds, B.C., Frank, M., Halliday, A.N., 2006b. New sample preparation techniques for the determination of Si isotopic compositions using MC-ICPMS. Chem. Geol. 235 (1), 95–104. https://doi.org/10.1016/j.chemgeo.2006.06.006.

Georg, R.B., Reynolds, B.C., West, A.J., Burton, K.W., Halliday, A.N., 2007. Silicon isotope variations accompanying basalt weathering in Iceland. Earth Planet. Sci. Lett. 261 (3), 476–490. https://doi.org/10.1016/j.epsl.2007.07.004.

Gislason, S.R., Arnorsson, S., Armannsson, H., 1996. Chemical weathering of basalt in Southwest Iceland; effects of runoff, age of rocks and vegetative/glacial cover. Am. J. Sci. 296 (8), 837–907. https://doi.org/10.2475/ajs.296.8.837.

Godsey, S.E., Kirchner, J.W., Clow, D.W., 2009. Concentration–discharge relationships reflect chemostatic characteristics of US catchments. Hydrol. Process. 23 (13), 1844–1864. https://doi.org/10.1002/hyp.7315.

Golla, J.K., Kuessner, M.L., Henehan, M.J., Bouchez, J., Rempe, D.M., Druhan, J.L., 2021. The evolution of lithium isotope signatures in fluids draining actively weathering hillslopes. Earth Planet. Sci. Lett. 567, 116988. https://doi.org/10.1016/j.epsl.2021.116988.

Golla, J.K., Bouchez, J., Druhan, J.L., 2024. Antecedent hydrologic conditions reflected in stream lithium isotope ratios during storms. Geophys. Res. Lett. 51 (17). https://doi.org/10.1029/2024gl109624.

Hall, F.R., 1970. Dissolved solids-discharge relationships: 1. Mixing models. Water Resour. Res. 6 (3), 845–850. https://doi.org/10.1029/WR006i003p00845.

Hall, F.R., 1971. Dissolved solids-discharge relationships: 2. applications to field data. Water Resour. Res. 7 (3), 591–601. https://doi.org/10.1029/wr007i003p00591.

Harman, C.J., 2015. Time-variable transit time distributions and transport: theory and application to storage-dependent transport of chloride in a watershed. Water Resour. Res. 51 (1), 1–30. https://doi.org/10.1002/2014wr015707.

Harman, C.J., Kim, M., 2014. An efficient tracer test for time-variable transit time distributions in periodic hydrodynamic systems. Geophys. Res. Lett. 41 (5), 1567–1575. https://doi.org/10.1002/2013gl058980.

Hrachowitz, M., Benettin, P., Van Breukelen, B.M., Fovet, O., Howden, N.J.K., Ruiz, L., Wade, A.J., 2016. Transit times—The link between hydrology and water quality at the catchment scale. WIREs Water 3 (5), 629–657. https://doi.org/10.1002/wat2.1155.

Hrachowitz, M., Fovet, O., Ruiz, L., Savenije, H.H.G., 2015. Transit time distributions, legacy contamination and variability in biogeochemical 1/fα scaling: how are hydrological response dynamics linked to water quality at the catchment scale? Hydrol. Process. 29 (25), 5241–5256. https://doi.org/10.1002/hyp.10546.

Hughes, H.J., Sondag, F., Santos, R.V., André, L., Cardinal, D., 2013. The riverine silicon isotope composition of the Amazon Basin. Geochim. Cosmochim. Acta 121, 637–651. https://doi.org/10.1016/j.gca.2013.07.040.

Ibarra, D.E., Caves, J.K., Moon, S., Thomas, D.L., Hartmann, J., Chamberlain, C.P., Maher, K., 2016. Differential weathering of basaltic and granitic catchments from concentration–discharge relationships. Geochim. Cosmochim. Acta 190, 265–293. https://doi.org/10.1016/j.gca.2016.07.006.

Intergovernmental Panel on Climate, C., 2023. Climate Change 2021 – The Physical Science Basis: Working Group I Contribution to the Sixth Assessment Report of the Intergovernmental Panel On Climate Change. Cambridge University Press. https://doi.org/10.1017/9781009157896.

Jasechko, S., Kirchner, J.W., Welker, J.M., McDonnell, J.J., 2016. Substantial proportion of global streamflow less than three months old. Nat. Geosci. 9 (2), 126–129. https://doi.org/10.1038/ngeo2636.

Kim, M. (2018). *Processes and landscape structure underlying system scale hydrologic transport: theory, experiment, and modeling* Johns Hopkins University. http://jhir.library.jhu.edu/handle/1774.2/60123.

Kim, M., Harman, C.J., 2022. Transit times and storage selection functions in idealized hillslopes with steady infiltration. Water Resour. Res. 58 (5). https://doi.org/10.1029/2019wr025917.

Kim, M., Troch, P.A., 2020. Transit time distributions estimation exploiting flow-weighted time: theory and proof-of-concept. Water Resour. Res. 56 (12). https://doi.org/10.1029/2020wr027186.

Kim, M., Volkmann, T.H.M., Bugaj, A., Wang, Y., Meira Neto, A.A., Matos, K., Troch, P. A., 2021. Uncovering the hillslope scale flow and transport dynamics in an experimental hydrologic system. Hydrol. Process. 35 (8), e14337. https://doi.org/10.1002/hyp.14337.

Kim, M., Volkmann, T.H.M., Wang, Y., Meira Neto, A.A., Matos, K., Harman, C.J., Troch, P.A., 2022. Direct observation of hillslope scale storage selection functions in experimental hydrologic systems: geomorphologic structure and preferential discharge of old water. Water Resour. Res. 58 (3). https://doi.org/10.1029/2020wr028959.

Kirchner, J., Feng, X., Neal, C., 2000. Fractal stream chemistry and its Implications for contaminant transport in catchments. Nature 403, 524–527. https://doi.org/10.1038/35000537.

Kirchner, J., Feng, X., Neal, C., 2001. Catchment-scale advection and dispersion as a mechanism for fractal scaling in stream tracer concentrations. J. Hydrol. 254, 82–101. https://doi.org/10.1016/S0022-1694(01)00487-5.

Kirchner, J.W., 2016a. Aggregation in environmental systems – Part 1: seasonal tracer cycles quantify young water fractions, but not mean transit times, in spatially heterogeneous catchments. Hydrol. Earth Syst. Sci. 20 (1), 279–297. https://doi.org/10.5194/hess-20-279-2016.

Kirchner, J.W., 2016b. Aggregation in environmental systems – Part 2: catchment mean transit times and young water fractions under hydrologic non stationarity. Hydrol. Earth Syst. Sci. 20 (1), 299–328. https://doi.org/10.5194/hess-20-299-2016.

Kirchner, J.W., Neal, C., 2013. Universal fractal scaling in stream chemistry and its implications for solute transport and water quality trend detection. Proc. Natl. Acad. Sci. 110 (30), 12213–12218. https://doi.org/10.1073/pnas.1304328110.

Knapp, J.L.A., Neal, C., Schlumpf, A., Neal, M., Kirchner, J.W., 2019. New water fractions and transit time distributions at Plynlimon, Wales, estimated from stable water isotopes in precipitation and streamflow. Hydrol. Earth Syst. Sci. 23 (10), 4367–4388. https://doi.org/10.5194/hess-23-4367-2019.

Li, L., Sullivan, P.L., Benettin, P., Cirpka, O.A., Bishop, K., Brantley, S.L., Kirchner, J.W., 2021. Toward catchment hydro-biogeochemical theories. WIREs Water 8 (1). https://doi.org/10.1002/wat2.1495.

Lutz, S.R., Krieg, R., Müller, C., Zink, M., Knöller, K., Samaniego, L., Merz, R., 2018. Spatial patterns of water age: using young water fractions to improve the characterization of transit times in contrasting catchments. Water Resour. Res. 54 (7), 4767–4784. https://doi.org/10.1029/2017wr022216.

Mackenzie, F.T., Garrels, R.M., 1966. Chemical mass balance between rivers and oceans. Am. J. Sci. 264 (7), 507–525.

Maher, K., 2010. The dependence of chemical weathering rates on fluid residence time. Earth Planet. Sci. Lett. 294 (1), 101–110. https://doi.org/10.1016/j.epsl.2010.03.010.

Maher, K., 2011. The role of fluid residence time and topographic scales in determining chemical fluxes from landscapes. Earth Planet. Sci. Lett. 312 (1), 48–58. https://doi.org/10.1016/j.epsl.2011.09.040.

Marçais, J., Derry, L.A., Guillaumot, L., Aquilina, L., De Dreuzy, J.R., 2022. Dynamic contributions of stratified groundwater to streams controls seasonal variations of stream water transit times. Water Resour. Res. 58 (3). https://doi.org/10.1029/2021wr029659.

Mcclain, M.E., Boyer, E.W., Dent, C.L., Gergel, S.E., Grimm, N.B., Groffman, P.M., Pinay, G., 2003. Biogeochemical hot spots and hot moments at the interface of terrestrial and aquatic ecosystems. Ecosystems 6 (4), 301–312. https://doi.org/10.1007/s10021-003-0161-9.

Mcguire, K.J., Mcdonnell, J.J., Weiler, M., Kendall, C., Mcglynn, B.L., Welker, J.M., Seibert, J., 2005. The role of topography on catchment-scale water residence time. Water Resour. Res. 41 (5). https://doi.org/10.1029/2004wr003657 n/a-n/a.

Millot, R., Gaillardet, J., Dupré, B., Allègre, C.J., 2002. The global control of silicate weathering rates and the coupling with physical erosion: new insights from rivers of the Canadian Shield. Earth Planet. Sci. Lett. 196 (1), 83–98. https://doi.org/10.1016/S0012-821X(01)00599-4.

Millot, R., Vigier, N., Gaillardet, J., 2010. Behaviour of lithium and its isotopes during weathering in the Mackenzie Basin, Canada. Geochim. Cosmochim. Acta 74, 3897–3912.

Oliva, P., Viers, J., Dupré, B., 2003. Chemical weathering in granitic environments. Chem. Geol. 202 (3), 225–256. https://doi.org/10.1016/j.chemgeo.2002.08.001.

Opfergelt, S., Cardinal, D., André, L., Delvigne, C., Bremond, L., Delvaux, B., 2010. Variations of δ30Si and Ge/Si with weathering and biogenic input in tropical basaltic ash soils under monoculture. Geochim. Cosmochim. Acta 74 (1), 225–240. https://doi.org/10.1016/j.gca.2009.09.025.

Opfergelt, S., de Bournonville, G., Cardinal, D., André, L., Delstanche, S., Delvaux, B., 2009. Impact of soil weathering degree on silicon isotopic fractionation during adsorption onto iron oxides in basaltic ash soils, Cameroon. Geochim. Cosmochim. Acta 73 (24), 7226–7240. https://doi.org/10.1016/j.gca.2009.09.003.

Opfergelt, S., Delmelle, P., 2012. Silicon isotopes and continental weathering processes: assessing controls on Si transfer to the ocean. Comptes Rendus Géosci. 344 (11–12), 723–738. https://doi.org/10.1016/j.crte.2012.09.006.

Opfergelt, S., Delvaux, B., André, L., Cardinal, D., 2008. Plant silicon isotopic signature might reflect soil weathering degree. Biogeochemistry 91 (2/3), 163–175.

Pangle, L.A., Delong, S.B., Abramson, N., Adams, J., Barron-Gafford, G.A., Breshears, D. D., Zeng, X., 2015. The landscape evolution observatory: a large-scale controllable infrastructure to study coupled earth-surface processes. Geomorphology 244, 190–203. https://doi.org/10.1016/j.geomorph.2015.01.020.

Pohlmann, M., Dontsova, K., Root, R., Ruiz, J., Troch, P., Chorover, J., 2016. Pore water chemistry reveals gradients in mineral transformation across a model basaltic hillslope. Geochem. Geophys. Geosyst. 17 (6), 2054–2069. https://doi.org/10.1002/2016gc006270.

Poitrasson, F., 2017. Silicon isotope geochemistry. Rev. Min. Geochem. 82 (1), 289–344. https://doi.org/10.2138/rmg.2017.82.8.

Preston, S.D., Bierman Jr, V.J., Silliman, S.E., 1989. An evaluation of methods for the estimation of tributary mass loads. Water Resour. Res. 25 (6), 1379–1389. https://doi.org/10.1029/WR025i006p01379.

Pringle, E.A., Moynier, F., Savage, P.S., Badro, J., Barrat, J.-A., 2014. Silicon isotopes in angrites and volatile loss in planetesimals. Proc. Natl. Acad. Sci. 111 (48), 17029–17032. https://doi.org/10.1073/pnas.1418889111.

Raymo, M.E., Ruddiman, W.F., 1992. Tectonic forcing of late Cenozoic climate. Nature 359 (6391), 117–122. https://doi.org/10.1038/359117a0.

Rinaldo, A., Benettin, P., Harman, C.J., Hrachowitz, M., Mcguire, K.J., Van Der Velde, Y., Botter, G., 2015. Storage selection functions: a coherent framework for quantifying how catchments store and release water and solutes. Water Resour. Res. 51 (6), 4840–4847. https://doi.org/10.1002/2015wr017273.

Robinson, J.S., Sivapalan, M., 1996. Instantaneous response functions of overland flow and subsurface stormflow for catchment models. Hydrol. Process. 10 (6), 845–862. https://doi.org/10.1002/(SICI)1099-1085(199606)10:6<845::AID-HYP375>3.0.CO;2-7.

Roerdink, D.L., van den Boorn, S.H.J.M., Geilert, S., Vroon, P.Z., van Bergen, M.J., 2015. Experimental constraints on kinetic and equilibrium silicon isotope fractionation during the formation of non-biogenic chert deposits. Chem. Geol. 402, 40–51. https://doi.org/10.1016/j.chemgeo.2015.02.038.

Savage, P.S., Georg, R.B., Armytage, R.M.G., Williams, H.M., Halliday, A.N., 2010. Silicon isotope homogeneity in the mantle. Earth Planet. Sci. Lett. 295 (1), 139–146. https://doi.org/10.1016/j.epsl.2010.03.035.

Soulsby, C., Birkel, C., Geris, J., Dick, J., Tunaley, C., Tetzlaff, D., 2015. Stream water age distributions controlled by storage dynamics and nonlinear hydrologic connectivity: modeling with high-resolution isotope data. Water Resour. Res. 51 (9), 7759–7776. https://doi.org/10.1002/2015wr017888.

Stallard, R.F., 1985. River chemistry, geology, geomorphology, and soils in the Amazon and Orinoco Basins. The Chemistry of Weathering. Springer Netherlands, pp. 293–316. https://doi.org/10.1007/978-94-009-5333-8_17.

Stallard, R.F., Edmond, J.M., 1983. Geochemistry of the Amazon: 2. The influence of geology and weathering environment on the dissolved load. J. Geophys. Res.: Oceans 88 (C14), 9671–9688. https://doi.org/10.1029/jc088ic14p09671.

Stallard, R.F., Edmond, J.M., 1987. Geochemistry of the Amazon: 3. Weathering chemistry and limits to dissolved inputs. J. Geophys. Res.: Oceans 92 (C8), 8293–8302. https://doi.org/10.1029/jc092ic08p08293.

Sun, L., Wu, L.H., Ding, T.P., Tian, S.H., 2008. Silicon isotope fractionation in rice plants, an experimental study on rice growth under hydroponic conditions. Plant Soil 304 (1), 291–300. https://doi.org/10.1007/s11104-008-9552-1.

Sun, Y., Wu, L.-H., Li, X.-Y., 2016. Experimental determination of silicon isotope fractionation in rice. PLoS One 11 (12), e0168970. https://doi.org/10.1371/journal.pone.0168970.

Tetzlaff, D., Birkel, C., Dick, J., Geris, J., Soulsby, C., 2014. Storage dynamics in hydropedological units control hillslope connectivity, runoff generation, and the evolution of catchment transit time distributions. Water Resour. Res. 50 (2), 969–985. https://doi.org/10.1002/2013wr014147.

Urey, H.C., Korff, S.A., 1952. The planets: their origin and development. Phys. Today 5 (8), 12.

van den Boorn, S.H.J.M., Vroon, P.Z., van Belle, C.C., van der Wagt, B., Schwieters, J., van Bergen, M.J., 2006. Determination of silicon isotope ratios in silicate materials by high-resolution MC-ICP-MS using a sodium hydroxide sample digestion method [10.1039/B600933F]. J. Anal. At. Spectrom. 21 (8), 734–742. https://doi.org/10.1039/B600933F.

Van Den Heuvel, D.B., Troch, P.A., Booij, M.J., Niu, G.Y., Volkmann, T.H.M., Pangle, L. A., 2018. Effects of differential hillslope-scale water retention characteristics on rainfall–runoff response at the landscape evolution observatory. Hydrol. Process. 32 (13), 2118–2127. https://doi.org/10.1002/hyp.13148.

Van Der Velde, Y., De Rooij, G.H., Rozemeijer, J.C., Van Geer, F.C., Broers, H.P., 2010. Nitrate response of a lowland catchment: on the relation between stream concentration and travel time distribution dynamics. Water Resour. Res. 46 (11). https://doi.org/10.1029/2010wr009105 n/a-n/a.

Volkmann, T.H.M., Sengupta, A., Pangle, L.A., Dontsova, K., Barron-Gafford, G.A., Harman, C.J., Troch, P.A., 2018. Controlled experiments of hillslope coevolution at the biosphere 2 landscape evolution observatory: toward prediction of coupled hydrological, biogeochemical, and ecological change. Hydrology of Artificial and Controlled Experiments. InTech. https://doi.org/10.5772/intechopen.72325.

Von Freyberg, J., Allen, S.T., Seeger, S., Weiler, M., Kirchner, J.W., 2018. Sensitivity of young water fractions to hydro-climatic forcing and landscape properties across 22 Swiss catchments. Hydrol. Earth Syst. Sci. 22 (7), 3841–3861. https://doi.org/10.5194/hess-22-3841-2018.

Walker, J.C., Hays, P., Kasting, J.F., 1981. A negative feedback mechanism for the long-term stabilization of Earth's surface temperature. J. Geophys. Res.: Oceans 86 (C10), 9776–9782.

Wang, W., Wei, H.-Z., Jiang, S.-Y., Liu, X., Lei, F., Lin, Y.-B., Zhao, Y., 2019. Silicon isotope geochemistry: fractionation linked to silicon complexations and its geological applications. Molecules 24 (7), 1415. https://doi.org/10.3390/molecules24071415.

White, A.F., Blum, A.E., Bullen, T.D., Vivit, D.V., Schulz, M., Fitzpatrick, J., 1999. The effect of temperature on experimental and natural chemical weathering rates of granitoid rocks. Geochim. Cosmochim. Acta 63 (19), 3277–3291. https://doi.org/10.1016/S0016-7037(99)00250-1.

White, T., Brantley, S., Banwart, S., Chorover, J., Dietrich, W., Derry, L., Lohse, K., Anderson, S., Aufdendkampe, A., Bales, R., Kumar, P., Richter, D., McDowell, B., 2015. The role of critical zone observatories in critical zone science. Develop. Earth Surf. Process. 19, 15–78. https://doi.org/10.1016/B978-0-444-63369-9.00002-1.

White, A.F., Schulz, M.S., Lawrence, C.R., Vivit, D.V., Stonestrom, D.A., 2017. Long-term flow-through column experiments and their relevance to natural granitoid weathering rates. Geochim. Cosmochim. Acta 202, 190–214. https://doi.org/10.1016/j.gca.2016.11.042.

Wilusz, D.C., Harman, C.J., Ball, W.P., 2017. Sensitivity of catchment transit times to rainfall variability under present and future climates. Water Resour. Res. 53 (12), 10231–10256. https://doi.org/10.1002/2017wr020894.

Yanhe, L., Tiping, D., Defang, W., 1995. Experimental study of silicon isotope dynamic fractionation and its application in geology. Chin. J. Geochem. 14 (3), 212–219. https://doi.org/10.1007/bf02842044.

Ziegler, K., Chadwick, O.A., Brzezinski, M.A., Kelly, E.F., 2005a. Natural variations of δ30Si ratios during progressive basalt weathering, Hawaiian Islands. Geochim. Cosmochim. Acta 69 (19), 4597–4610. https://doi.org/10.1016/j.gca.2005.05.008.

Ziegler, K., Chadwick, O.A., White, A.F., Brzezinski, M.A., 2005b. δ30Si systematics in a granitic saprolite, Puerto Rico. Geology 33 (10), 817–820. https://doi.org/10.1130/g21707.1.